

Sum-frequency generation in bound-state-in-continuum microring resonators

FAN YE, XIANKAI SUN,  AND HON KI TSANG* 

Department of Electronic Engineering, The Chinese University of Hong Kong, Shatin, New Territories, Hong Kong SAR, China
*hktsang@ee.cuhk.edu.hk

Received 11 March 2025; revised 8 May 2025; accepted 26 May 2025; posted 27 May 2025; published 11 June 2025

Bound states in the continuum (BICs) can facilitate strong optical mode confinement for nonlinear optical applications. Recently, BICs were used for low-loss photonic integrated circuits, enabling waveguides to be fabricated without etching on material platforms which do not have mature low-loss etching processes. Here, we show experimentally that the losses in BIC microring resonators are sufficiently low for efficient sum-frequency generation (SFG) on an etchless lithium niobate platform. The normalized conversion efficiency is measured to be $6.45 \times 10^{-6} \text{ mW}^{-1}$. These results establish the feasibility of this approach for exploring the use of what we believe to be novel functional materials for nonlinear integrated photonics. © 2025 Optica Publishing Group. All rights, including for text and data mining (TDM), Artificial Intelligence (AI) training, and similar technologies, are reserved.

<https://doi.org/10.1364/OL.561879>

Bound state in the continuum (BIC) is a perfectly confined state that exists exceptionally in the continuum and exhibits no radiation loss. Recently, it was proposed and demonstrated that photonic BICs can exist in a low-refractive-index waveguide on a high-refractive-index substrate [1,2]. The destructive interference among various loss channels suppresses energy dissipation in the BIC-based waveguide, resulting in theoretically zero propagation loss. The BIC mechanism introduces a novel approach to make photonic integrated circuits (PICs) without conventional etching of the high-refractive-index materials.

Lithium niobate on insulator (LNOI) platform is frequently used for PICs because of its excellent characteristics, such as wide transparency window, low optical absorption, high refractive index, as well as strong electro-optic, piezoelectric, acousto-optic, and second-order nonlinear effects. The photonic BIC mechanism enables the use of its attractive optical properties without etching and has been demonstrated in acousto-optic modulation [3,4], electro-optic modulation [2,5–7], second-harmonic generation (SHG) [8,9], and quantum light sources [10]. This BIC-based integrated platform can also facilitate the integration of high-refractive-index materials with useful functional properties. For example, when integrated with 2D materials, the platform can achieve photodetection, modulation, and light emission [11–13].

Second-order nonlinear optical effects including SHG and spontaneous parametric downconversion (SPDC) have been demonstrated using BIC integrated waveguides. Sum-frequency

generation (SFG) is a significant application of second-order nonlinear susceptibility. As a three-wave mixing nonlinear process of upconversion [14–18], SFG has established its importance in frequency conversion applications. Unlike SHG and SPDC processes, SFG uniquely enables the conversion of weak low-frequency optical signals to higher-frequency optical signals through the utilization of a high-intensity optical pump. Notably, this conversion process preserves quantum states, making it particularly valuable for applications in quantum frequency conversion and single-photon detection systems [19–21].

Previously an integrated quantum source utilizing the BIC [10] was reported, but it remained unclear whether the necessary phase-matching could be achieved for efficient SFG to be realized on the BIC-based platform for integrated quantum frequency conversion, thereby improving the integration density of quantum photonic chips. The BIC mode enables the study of long optical interaction lengths with any new optical materials using a simple etchless fabrication method. For example, it can be adopted to the heterogeneous integration of optically active materials, including perovskites, two-dimensional transition metal dichalcogenides, and quantum-dot-doped polymers, offering promising avenues for constructing efficient single-photon sources and integration of hybrid integrated photodetectors and modulators. In this study, we explore whether efficient SFG utilizing BICs can be possible.

We designed the BIC microring resonator for SFG, utilizing the modal phase-matching (MPM) method. The realization of efficient SFG in microresonators is challenging, primarily because of the stringent requirements for fabricating a microresonator that simultaneously exhibits triple resonances at precisely matched frequencies for both energy conservation and phase-matching at the different frequencies. Our experimental results demonstrate an SFG conversion efficiency of $6.45 \times 10^{-6} \text{ mW}^{-1}$. The SFG signal, designed as a BIC mode, exhibits a linear power dependence on the pump power, consistent with theoretical predictions. Furthermore, we have systematically investigated and characterized the relationship between the SFG power and one of the pump wavelengths.

The SFG microring resonator was fabricated on a z-cut lithium niobate (LN) thin film bonded to a 2- μm -thick thermally grown silicon dioxide layer on a silicon substrate (NANOLN Inc.). Figure 1(a) illustrates the cross-sectional structure of this etchless device. The top layer consists of a low-refractive-index material. In this work, we employed a polymer for the top layer, specifically an electron-beam resist (ZEP520A), which can be

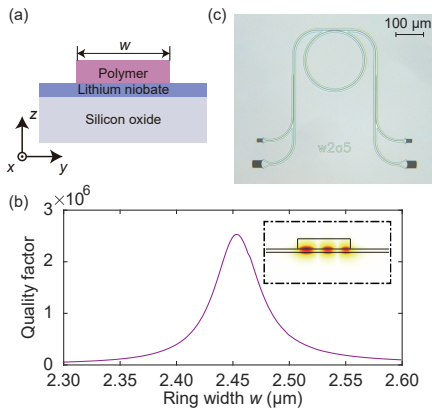


Fig. 1. (a) Cross-sectional illustration of the waveguide structure which consists of a polymer waveguide on top of a LNOI substrate. (b) Quality factor of the TM_{20} mode as a function of the ring width w . (c) Optical microscope image of a fabricated BIC microring resonator device.

nanostructured solely through electron-beam lithography and development. Beneath this layer lies the high-refractive-index LN film, which eliminates the need for conventional etching processes. This configuration supports modes with diverse polarizations across two distinct wavelength ranges. However, to achieve an ultralow-loss BIC mode, the TM mode of the microring structure is essential.

The interaction between the bound and continuous modes originates from the two edges of the bent waveguide, characterized by unequal dissipation rates through these channels. The total dissipation rate of the TM bound mode to the TE continuum in the high-refractive-index slab can be estimated using $|J_q(n_b k_r R) - \gamma J_q(n_b k_r (R - w_b))|$ [22], where J_q represents the q th-order Bessel function, n_b is the refractive index of the bent waveguide, k_r is the wave vector along the radial direction, R is the bend radius of the outer waveguide edge, w_b is the bent waveguide width, and γ is the ratio of electric field amplitudes of the TM bound mode at the inner and outer waveguide edges.

The coupling loss is primarily determined by three parameters: bent waveguide width, bend radius, and the ratio of electric field amplitudes γ . When the loss is zero, theoretically the lossless BIC mode is obtained. The primary determinant of the BIC point changes from bend radius R to bent waveguide width w_b when γ varies from 0 to 1. Here $\gamma = 0$ corresponds to the special case of a microdisk structure, while $\gamma = 1$ corresponds to a waveguide structure. In microring structures, as the ring radius increases, γ approaches 1, indicating that the bent waveguide width becomes a more important factor influencing the position of the lossless BIC point. This transition underscores the critical role of waveguide geometry in determining the BIC mode.

Meanwhile, to achieve efficient wavelength conversion between the pump wavelength and signal wavelength, the MPM condition must be fulfilled. Therefore, we selected the TE_{00} mode for the pump light and the TM_{20} mode at a near-visible wavelength. A larger ring radius is also employed to ensure the MPM. The inset of Fig. 1(b) depicts the electric field ($|E|$) profile of the TM_{20} mode. We set the ring radius at $102 \mu\text{m}$, where the lossless BIC condition mainly depends on the ring width. The simulated quality factor of the TM_{20} mode as a function of the ring width is shown in Fig. 1(b). The TM_{20} mode achieves

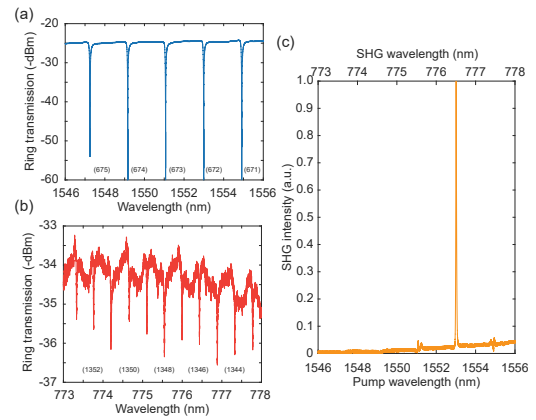


Fig. 2. (a) Measured transmission spectrum of the microring resonator in the pump wavelength range. (b) Measured transmission spectrum of the microring resonator in the second-harmonic wavelength range. (c) Measured normalized SHG spectrum of the microring resonator.

its maximal quality factor at a ring width of $2.45 \mu\text{m}$, which we call the BIC point.

The entire fabricated device comprises a microring resonator for SFG, two pairs of grating couplers for coupling light onto and out of the chip, and directional couplers for (de)multiplexing the SFG ($\sim 776.5 \text{ nm}$ wavelength) light and the pump (1553 nm) light. The measured coupling losses including the directional couplers are 11.5 dB at 1553 nm and 18.0 dB at 776.5 nm . Figure 1(c) shows an optical microscope image of a fabricated BIC microring resonator device.

In the experiment, we first performed linear transmission measurement of the fabricated microring resonator. The free spectral range (FSR) of the resonant TE_{00} mode in the pump wavelength range is $\sim 1.92 \text{ nm}$, while the FSR of the resonant TM_{20} mode in the second-harmonic (SH) wavelength range is $\sim 0.44 \text{ nm}$. The transmission spectra, which characterize the optical modes of the microring resonator at both pump and SH wavelengths, are illustrated in Figs. 2(a) and 2(b), respectively. By Lorentzian fitting, the Q factor of the resonance “672” in the pump wavelength range is calculated to be 2.2×10^4 , while the resonance “1346” in the SH wavelength range exhibits a Q factor of 4.2×10^4 . The difference between the measured and simulated Q factors is due to material absorption and fabrication-induced scattering losses. The experimental Q factor may be improved further by replacing the polymer with other low-refractive-index materials (e.g., SiO_2), which nowadays have mature recipes for producing nanostructures with high quality.

We then characterized the device with degenerate pumping for SHG using the TE mode at telecom wavelength and the TM_{20} mode at near-visible wavelength. The maximal normalized SHG conversion efficiency reached $3.23 \times 10^{-6} \text{ mW}^{-1}$ near the phase-matching point. Figure 2(c) shows the measured SHG conversion spectrum, which suggests that the phase-matching condition is best satisfied when the pump mode is resonance “672” at $\sim 1553 \text{ nm}$. Notably, the phase-matching condition is significantly compromised when the pump light is tuned to resonance “671” or “673” and completely unattainable at other wavelengths.

The modal overlap factor ξ between the TE_{00} mode at the fundamental wavelength and the TM_{20} mode at the

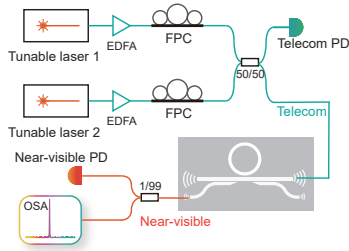


Fig. 3. Experimental setup for the SFG measurement. EDFA, erbium-doped fiber amplifier; FPC, fiber polarization controller; PD, photodetector; OSA, optical spectrum analyzer.

second-harmonic wavelength is expressed as [23]

$$\xi = \frac{\left(\iint drdz |u_{p,r}^*(r, z)|^2 |u_{SH,z}(r, z)|^2 \right)^3}{\iint drdz |u_{p,z}(r, z)|^2 \cdot \sqrt{\iint drdz |u_{SH,z}(r, z)|^2}}, \quad (1)$$

where $u(r, z)$ is the electric field component of the cavity mode at the respective wavelength, with its attributes in the subscript denoting the pump (p) or second-harmonic (SH) mode in the radial (r) or vertical (z) direction. For the measured resonant modes, we obtained a numerically simulated ξ of $0.14/\mu\text{m}$. A larger overlap factor can lead to a higher nonlinear conversion efficiency. Ways of improving the overlap factor include adopting a fundamental mode instead of the $1M_{20}$ mode as the second-harmonic mode and adopting the $1M_{00}$ mode instead of the $1E_{00}$ mode as the pump mode [8].

Figure 3 illustrates the experimental setup for the SFG experiment. Two pump light beams, denoted as Pump 1 and Pump 2, are from two continuous-wave tunable semiconductor lasers at telecom wavelengths. Both pump sources were individually amplified with an erbium-doped fiber amplifier before being combined with a 50/50 fiber splitter. The combined light was subsequently coupled into the device under the test as the pump source. After dividing by the on-chip wavelength demultiplexer, the signal light was extracted from the device through a specifically designed grating coupler and collected by a highly sensitive InGaAs photodetector for SFG signal measurement.

In second-order nonlinear optical processes, the phase-matching condition [24] can be expressed as $n_1\omega_1 + n_2\omega_2 = n_3\omega_3$, where n_i is the effective refractive index of the i th mode and ω_i is the corresponding frequency. The left-hand side of the equation is usually for the pump, while the right-hand side for the generated nonlinear signal, where the energy conservation condition $\omega_1 + \omega_2 = \omega_3$ also has to be satisfied. In the specific case of SHG, where $\omega_1 = \omega_2$ and $\omega_3 = 2\omega_1 = 2\omega_2$, the phase-matching condition is simplified to $n_1 = n_2 = n_3$. For the more general scenario of SFG where $\omega_1 \neq \omega_2$, the phase-matching condition can be achieved when ω_1 and ω_2 are symmetrically distributed around the phase-matching point and maintain close proximity. This is feasible because the mode dispersion can be approximated as linear in this regime.

Based on previous measurements, we could successfully observe SHG when the pump was tuned to resonances “671,” “672,” and “673.” Notably, resonance “672” is the closest to the phase-matching point, while the phase-matching condition is significantly compromised at resonances “671” and “673.” According to the phase-matching equation, nondegenerate pumps at resonance “671” and “673,” which are symmetric

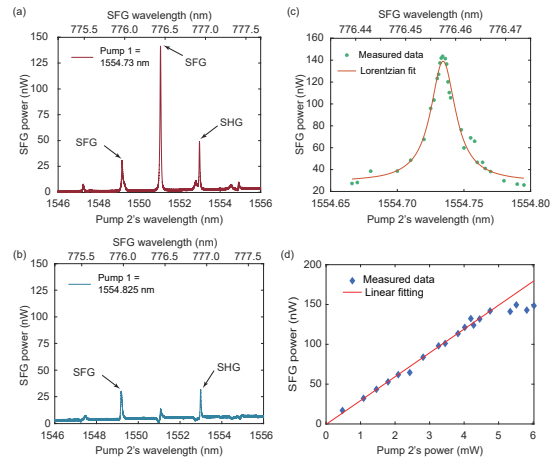


Fig. 4. (a), (b) Measured SFG spectra when the pump wavelength is (a) at and (b) away from the phase-matching point. (c) Measured (green dots) and Lorentzian fitted (red line) SFG power as a function of Pump 2’s wavelength with fixed power. (d) Measured (blue diamonds) and fitted (red line) SFG power as a function of Pump 2’s power in the bus waveguide.

with respect to resonance “672,” are expected to generate a more efficient SFG signal.

In the first SFG test, Pump 1 was stabilized at 1554.73 nm with constant power, near resonance “671.” Subsequently, Pump 2 was introduced into the microring resonator while maintaining its power at an equivalent level. Through wavelength sweep of Pump 2 and signal detection using a highly sensitive InGaAs photodetector, we acquired the power spectrum of the generated near-visible light, as illustrated by the red curve in Fig. 4(a). Based on our previous result in Fig. 2(a), we anticipated the phase-matching condition to be fulfilled near 1553 nm, which accounts for the presence of the side peak on the right, corresponding to the SHG signal of Pump 2 at ~ 1553 nm. When Pump 2 was tuned to 1551 nm, the highest peak occurred due to Pump 1 and Pump 2 being at resonances “671” and “673,” respectively, which are symmetric with respect to resonance “672,” the phase-matching point. This observation aligns with our prior assumptions, confirming that the SFG phase-matching is effectively achieved. The left-side peak represents the SFG signal generated by Pump 1 at resonance “671” and Pump 2 at resonance “674.” The reduced intensity of this peak can be attributed to the less optimal phase-matching condition of the pump combination.

Next, we adjusted the wavelength of Pump 1 to 1554.825 nm and still recorded the swept spectrum of Pump 2, as shown by the blue curve in Fig. 4(b). The observed right-side peak originates predominantly from the SHG signal of Pump 2 at ~ 1553 nm. Notably, when Pump 2 swept to resonance “673” again, the central SFG peak in Fig. 4(a) vanished due to off resonance. Figure 4(c) shows the recorded SFG power of the central peak as a function of Pump 2’s wavelength. The experimental data points, plotted as green dots, demonstrate that the strongest SFG signal occurs when Pump 2’s wavelength is 1554.73 nm. The red curve plots a Lorentzian fit to the experimental data.

Figure 4(d) shows the measured SFG signal power as a function of Pump 2’s power, under the condition of maximal SFG output. In this experiment, the wavelengths of Pump 1 and 2 were set at 1554.73 and 1551.07 nm, respectively. The on-chip

Table 1. Comparison of SFG with Microcavities on LNOI

Ref.	Structure	SFG Efficiency	Quality Factors ^a
[14]	Microdisk	$1.4 \times 10^{-7}/\text{mW}$	$3.7 \times 10^5/3.1 \times 10^5$ $1.8 \times 10^5/\text{expected to}$
[15]	Microdisk	$2.22 \times 10^{-6}/\text{mW}$	be equivalent
[25]	Microdisk	$6.15 \times 10^{-4}/\text{mW}$	$\sim 10^5$
[16]	Microdisk	$2.52 \times 10^{-4}/\text{mW}$	1.06×10^6
[26]	Microring	$5.9 \times 10^{-5}/\text{mW}$	1.3×10^4
This work	Microring	$6.45 \times 10^{-6}/\text{mW}$	$2.2 \times 10^4/4.2 \times 10^4$

^aFor a single value, it is the quality factor at the telecommunication wavelength. For double values, the first (second) one is the quality factor at the telecommunication (near-visible) wavelength.

power of Pump 1 was fixed at 4.62 mW, while Pump 2's power varied from 0.5 to 6 mW. Initially, the SFG power exhibited a linear relationship with Pump 2's power. However, when Pump 2's power exceeded 4.75 mW, the result of SFG signal exhibited a deviation from the linear dependence on Pump 2's power. This is due to the saturation effect in the SFG process and the onset of Pump 1's depletion when its power is exceeded by Pump 2. In this scenario, further increase in Pump 2's power is in vain. The SFG conversion efficiency, defined as $P_{\text{SFG}}/(P_1P_2)$ with P_{SFG} , P_1 , and P_2 being the power of the SFG signal, Pump 1, and Pump 2, respectively, was measured to be $6.45 \times 10^{-6} \text{ mW}^{-1}$ in our experiment. The SFG efficiency is better than SHG because of the better satisfaction of phase-matching condition with two nondegenerate pumps.

Table 1 compares the performance of SFG with microcavities on LNOI platform. Our work has higher quality factors than other microring structures. More importantly, our etchless scheme offers greater convenience and higher device yield in fabrication compared with the traditional methods that require LN etching. This approach demonstrates excellent adaptability and can readily be applied to other platforms incorporating novel materials.

In conclusion, we have successfully demonstrated efficient SHG and SFG in a BIC microring resonator. The measured conversion efficiencies reached $3.23 \times 10^{-6}/\text{mW}$ for SHG and $6.45 \times 10^{-6}/\text{mW}$ for SFG. The efficiencies can be further improved by using more efficient but more complicated phase-matching methods such as periodic poling. Our work shows the

potential of BIC structures for nonlinear integrated photonic applications. By leveraging these fundamental BIC integrated elements, researchers can explore nonlinear optical phenomena using advanced materials, paving the way for innovative applications in optical signal processing and integrated quantum photonic systems with enhanced functionality and performance.

Funding. Hong Kong UGC (Research Matching Grant Scheme RMGS-01).

Disclosures. The authors declare no conflicts of interest.

Data availability. The data that support the findings of this study are available from the corresponding author upon request.

REFERENCES

- C.-L. Zou, J.-M. Cui, F.-W. Sun, *et al.*, *Laser Photonics Rev.* **9**, 114 (2015).
- Z. Yu, X. Xi, J. Ma, *et al.*, *Optica* **6**, 1342 (2019).
- Z. Yu and X. Sun, *ACS Photonics* **8**, 798 (2021).
- Y. Yu, L. Wang, and X. Sun, *Nanophotonics* **10**, 4323 (2021).
- Z. Yu, Y. Tong, H. K. Tsang, *et al.*, *Nat. Commun.* **11**, 2602 (2020).
- J. Zhang, B. Pan, W. Liu, *et al.*, *Opt. Express* **30**, 20839 (2022).
- G. Liu, S. Zong, X. Liu, *et al.*, *Opt. Lett.* **49**, 113 (2024).
- F. Ye, Y. Yu, X. Xi, *et al.*, *Laser Photonics Rev.* **16**, 2100429 (2022).
- F. I. Baida, J. J. Robayo Yepes, and A. Ndao, *J. Appl. Phys.* **133**, 12 (2023).
- F. Ye, Y. Qin, C. Cui, *et al.*, *Photonics Res.* **12**, 1322 (2024).
- Z. Yu, Y. Wang, B. Sun, *et al.*, *Adv. Opt. Mater.* **7**, 1901306 (2019).
- X.-J. Liu, Y. Yu, D. Liu, *et al.*, *Nano Lett.* **23**, 3209 (2023).
- Y. Wang, Z. Yu, Z. Zhang, *et al.*, *ACS Photonics* **7**, 2643 (2020).
- Z. Hao, J. Wang, S. Ma, *et al.*, *Photonics Res.* **5**, 623 (2017).
- X. Ye, S. Liu, Y. Chen, *et al.*, *Opt. Lett.* **45**, 523 (2020).
- J. Zhu, X. Sun, T. Ding, *et al.*, *J. Opt. Soc. Am. B* **40**, D44 (2023).
- D. V. Strelakov, A. S. Kowligy, Y.-P. Huang, *et al.*, *New J. Phys.* **16**, 053025 (2014).
- Z. Li, B. Corbett, A. Gocalinska, *et al.*, *Light: Sci. Appl.* **9**, 180 (2020).
- J.-W. Chae, J.-H. Kim, Y.-C. Jeong, *et al.*, *Nanophotonics* **12**, 495 (2023).
- X. Wang, X. Jiao, B. Wang, *et al.*, *npj Quantum Inf.* **9**, 38 (2023).
- X.-S. Song, Z.-Y. Yu, Q. Wang, *et al.*, *Opt. Express* **19**, 380 (2011).
- Y. Yu and X. Sun, *J. Opt. Soc. Am. B* **40**, 2801 (2023).
- J. Lu, J. B. Surya, X. Liu, *et al.*, *Optica* **6**, 1455 (2019).
- R. V. Roussev, C. Langrock, J. R. Kurz, *et al.*, *Opt. Lett.* **29**, 1518 (2004).
- Z. Hao, L. Zhang, J. Wang, *et al.*, *Chin. Opt. Lett.* **20**, 111902 (2022).
- J. Wang, B. Wang, J. Qu, *et al.*, *Opt. Lett.* **50**, 2057 (2025).